A Geostationary Microwave Sounder: Design, Implementation and Performance

Bjorn Lambrigtsen ⓘ, Pekka Kangaslahti, Oliver Montes, Noppasin Niamsuwan, Derek Posselt ⓘ, Jacola Roman, Mathias Schreier, Alan Tanner, Longtao Wu, and Igor Yanovsky

Abstract—A geostationary microwave sounder, capable of providing continuous monitoring of temperature, water vapor, clouds, precipitation, and wind in the presence of clouds and precipitation is now feasible. A design called the Geostationary Synthetic Thinned Aperture Radiometer (GeoSTAR) has been developed at the Jet Propulsion Laboratory, and the required new technology has been developed and is sufficiently mature that a space mission can be initiated. GeoSTAR can be thought of as "AMSU in GEO," i.e., it has capabilities in geostationary earth orbit (GEO) similar to those of microwave sounders currently operating in low earth orbit. Having such a capability in GEO will add tremendously to our ability to observe dynamic atmospheric phenomena, such as hurricanes and severe storms, monsoonal moisture flow, and atmospheric rivers. GeoSTAR will make measurements every 15 min or less instead of every 12 h and cover a large portion of the Earth continuously instead of with snapshots in a narrow swath. By tracking water vapor patterns, it is also possible to derive atmospheric wind speed and direction at altitudes from the surface to 10–15 km. All of this can be done regardless of cloud cover and weather conditions. During the latter half of 2020, a detailed study of GeoSTAR and its projected performance was undertaken as one of several such studies commissioned by the National Oceanic and Atmospheric Administration (NOAA) for the purpose of configuring NOAA's next generation of earth environmental satellite systems. We present a summary of our findings, including instrument characteristics, measurement accuracy and precision, and expected impact on weather prediction and applications.

Index Terms—Atmospheric sounder, geostationary, microwave, observing system simulation experiments (OSSE), wind.

I. INTRODUCTION

DURING the latter half of 2020, a detailed study of a geostationary microwave sounder concept and its projected performance was undertaken at the Jet Propulsion Laboratory (JPL) as one of several such studies commissioned by the National Oceanic and Atmospheric Administration (NOAA) to assist in configuring NOAA's next generation of earth environmental and

weather satellite systems. Based on the Geostationary Synthetic Thinned Aperture Radiometer (GeoSTAR) concept developed at JPL, such a sounder is now feasible and will provide measurements similar to what are now obtained with the current low earth orbit (LEO) microwave sounders, the advanced microwave sounding unit (AMSU), and the advanced technology microwave sounder (ATMS), but every 15 min instead of every 12 h and covering a large fraction of a hemisphere instead of a narrow swath. Geostationary earth orbits (GEO) are almost 50 times higher than the LEO orbits that AMSU and ATMS operate from, and the corresponding scaling of aperture size required to maintain spatial resolution had stymied the development of such a sensor for many decades in spite of an expectation in the atmospheric science community that a geostationary microwave sounder would revolutionize the field. This was already noted in 1985 by Verner Suomi [1]: "The VAS experience suggests that extension into the microwave region, and increased spectral resolution in the infrared region, are essential so that we can obtain soundings through persistent clouds and with improved vertical resolution. Geostationary microwave instruments and high spectral resolution infrared interferometers are feasible and would be highly useful." The aperture synthesis approach implemented with GeoSTAR finally overcomes that obstacle, and the large number of microwave receivers and associated electronics required is made possible with new technology that has now been developed and fully tested in a "relevant environment" (in this case, on the ground) as required by NASA to verify appropriate technology readiness. The study determined that the performance of such a system will match, and in some areas exceed, the performance of AMSU and ATMS and will lead to significant improvements in both regional and global weather prediction by incorporating the crucial time dimension through continuous observations. It will also provide vertical profiles of atmospheric wind vectors under almost any weather condition, which many consider a breakthrough capability.

The first "Decadal Survey" of earth science missions for NASA [2] recommended that such a sensor be developed for a "Precipitation and All-weather Temperature and Humidity" (PATH) mission and recommended that it be implemented as an "array spectrometer." That was largely based on the GeoSTAR concept then under development at the Jet Propulsion Laboratory (JPL). At the time, the required technology was not sufficiently mature, and PATH was therefore put in the "third tier" group of missions that required further development. Under sponsorship from the NASA Earth Science Technology Office's (ESTO)

Instrument Incubator Program (IIP), the key technologies have been developed and have been brought to the Technology Readiness Level (TRL) 6 required by NASA for mission implementation, thus enabling the PATH mission [3].

The fundamental requirement was for the PATH sensor to provide temperature and water vapor sounding (i.e., generate vertical profiles) continuously, with a very rapid update cycle (15–30 min) and under nearly all weather conditions. The spatial resolution must be sufficient to resolve key storm-scale processes. Past research based on data from LEO sounders, such as the AMSU [4], [5], suggests that this can be achieved with the capabilities of those sensors if they were available in GEO. Thus, the PATH sensor could be viewed as "AMSU in GEO." This requires operating in the 50- or 118-GHz band for temperature sounding and in the 183-GHz band for water vapor sounding, as noted by the NRC. It also means attaining spatial resolution of about 25 km (similar to the 15–50 km of AMSU). Such a resolution is very difficult to achieve with a microwave sensor in GEO and has prevented the development of a GEO microwave (MW) system until now. For example, AMSU has an antenna aperture of about 15 cm, but scaled from LEO (830 km) to GEO (36 000 km), this becomes 6.5 m. Getting such an antenna into space while maintaining the surface precision required for sounding has been prohibitive, and scanning it across the earth disc is also a challenge. This problem has now finally been solved with the development of the GeoSTAR design and the technology required to implement it.

There has long been a strong interest in a geostationary microwave sounder, both in the research community and the weather forecasting community. Reliable forecasts of extreme-weather events would have substantial societal and economic benefits through disaster mitigation. GeoSTAR also has the ability to measure tropospheric wind as well as thermodynamic profiles under a wide range of weather conditions, and a GEO MW sounder would enable significant advances in this area. For example, the intensification of a hurricane is strongly affected by the vertical shear of tropospheric winds, and accurate tropical wind observations could provide improved tropical cyclone predictions. Despite the importance of accurate three-dimensional tropospheric winds, large uncertainties remain in the 3-D tropospheric wind analysis and reanalysis over the oceans, the tropics, the polar regions, and regions where ground-based radiosonde observations are scarce.

In the following sections, we describe the instrument and its measurement capabilities and the various aspects of performance assessment that were undertaken in the study for NOAA.

II. OBSERVING SYSTEM

A. Instrument Concept

The concept that forms the basis for GeoSTAR originated in 1998, when it was proposed to NASA in response to a solicitation of new ideas for geostationary observing systems, sponsored by the NASA New Millennium Program. Then called the Geostationary Synthetic Aperture Microwave Sounder (GEO/SAMS), it was selected as one of four concepts to go forward with Phase-A studies. Eventually, an infrared sounder concept (the
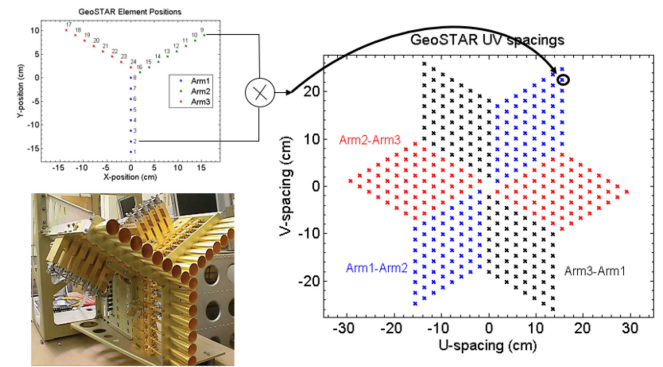

Fig. 1. "Y" array physical geometry and associated visibility function sampling geometry, also known as the "synthetic aperture." Also shown here is the first GeoSTAR demonstrator instrument which was completed in 2006 at JPL using this geometry.

Geostationary Infrared Fourier Transform Spectrometer) was selected for further development. Later, in 2003, the GeoSTAR concept was selected by ESTO for technology development under the Instrument Incubator Program. Two additional IIP awards followed, until all key technologies had been fully developed and tested by 2014–2015.

The GeoSTAR instrument employs the synthetic aperture radiometer techniques that were originally developed in the 1970s by radio astronomers to achieve extremely high spatial resolution imagery from a relatively small number of radio telescopes. The technique involves measuring the cross-correlation of radio signals received by pairs of antennas separated by known "baselines" of various orientations and separation distance. This measurement is referred to as the visibility function. When adequately sampled in two dimensions, the visibility function can be converted into a radiometric image by means of a Fourier Transform.

The visibility function, $V(u, v)$, is a complex function—meaning that there is a phase and magnitude associated with each visibility sample. The visibility function is conjugate symmetric, in that $V(u, v) = V^*(-u, -v)$ where the $*$ superscript denotes the conjugation operator. In Fig. 1, the u–v example grid is shown with $p = 8^2 \times 6 = 384$ samples, as formed between three arms of eight elements each. It is helpful to recognize that that there are also 384 independent variables measured in the array of Fig. 1 ($= 192$ in-phase $+ 192$ quadrature phase correlations). Because the Fourier Transform is a one-to-one mapping, the number of visibility samples also equals the number of independent "pixels" which are resolved in the synthesized image. In other words, N independent measurements go into the Fourier Transform, and N independent measurements always come out. We note that the reconstructed image is not actually a collection of pixels but is instead a smooth but blurred version of the true image, as represented by a finite Fourier series. The noise is distributed across the image per the equation shown in Fig. 2 and depends on N.

Fig. 1 includes a photograph of a JPL GeoSTAR demonstrator that was developed and tested extensively, in laboratories at JPL and at the NASA Goddard Space Flight
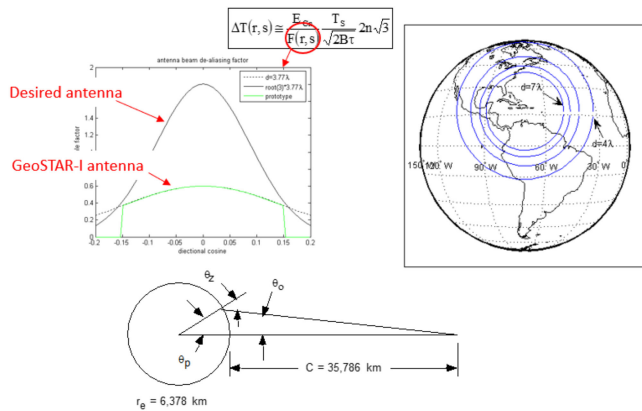
Fig. 2. Sensitivity of a synthesis array (upper left) improves when the antenna beam is concentrated on the desired image area [6]–[8]. $F(r,s)$ represents an antenna pattern normalized to the synthetic image area; E is a correlator efficiency term that is near unity; T_s is system noise temperature; B is bandwidth; τ is integration time; and n is the number of antenna elements in one arm of the array).

Fig. 3. "GeoStorm" design: A multirow array (left), resulting field of view (FOV; right).

Fig. 4. GeoSTAR prototype, operating at 183 GHz.

Center as well as outdoors, between 2003 and 2006 under the first of three IIP efforts. This first instrument was built as a proof-of-concept demonstrator. At the time, the European Soil Moisture and Ocean Salinity mission, which implements a STAR system operating in L-band, had not yet flown, and only a small number of one-dimensional airborne synthetic aperture radiometers—on much smaller scales—had shown success. Two-dimensional image synthesis in the context of Earth remote sensing needed to be demonstrated, and the tests of this first instrument fulfilled that need. This development also produced a wealth of practical lessons which guided subsequent instrument designs.

From the start of the first IIP development, the antenna element design—in this case, a horn antenna operating from 50 to 55 GHz—was a known and critical design consideration for a GEO observatory. Ideally, the antenna should place all of the antenna energy exclusively inside the desired image area. Such an antenna element is only possible with enough physical room for the aperture. Yet, as evident in Fig. 1, the physical separation between antenna elements in the array restricts the size of the antenna. The best antenna design placed only 40% of the antenna beam energy on the Earth. The remaining 60% is lost to cold space, representing a severe inefficiency. Fig. 2 illustrates the problem: The "desired" antenna element should have much greater antenna gain. This figure shows (upper left) the desired antenna function vs. the one designed for the initial prototype (note that the Earth disc extends to ± 0.15 in direction cosines seen from GEO). The lower element shows the geometry and associated angles, and the upper left shows the half-power antenna function contours projected on the Earth disc for various element spacings.

This problem was solved with a new antenna array design that has multiple parallel rows of receiving elements, which results in a narrower field of view (FOV) and sharp rejection of alias signals. An example is illustrated in Fig. 3. Here the overall FOV is about 1000 km. This is the so-called "GeoStorm" design. Fig. 4
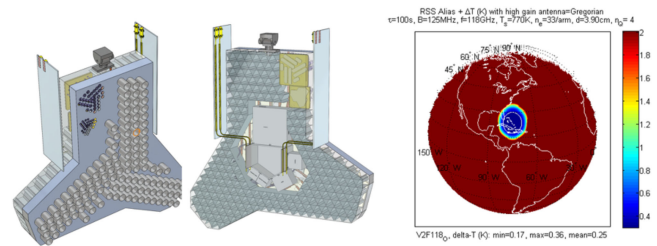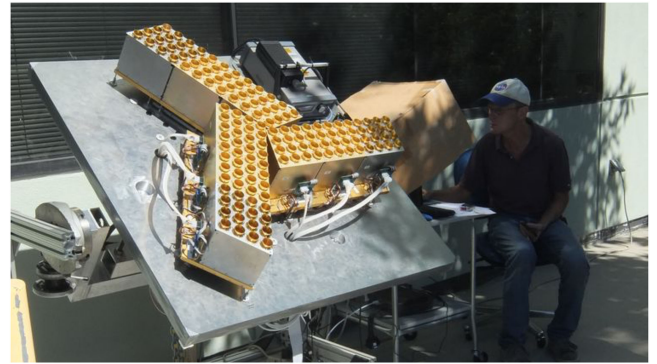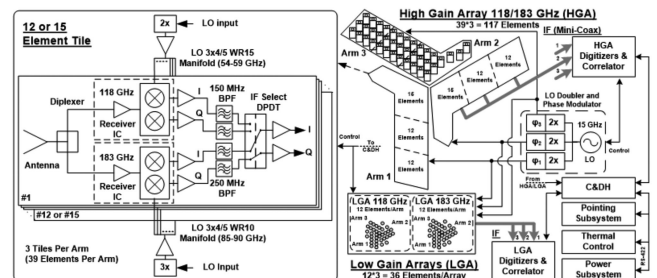

Fig. 5. Block diagram of the GeoStorm system.

shows a photo of a 1/3-scale demonstration model developed under the IIP program.

B. "GeoStorm" Baseline Design

Fig. 5 shows a block diagram of the GeoStorm implementation. It consists of a single "high-gain" array (HGA) of receiver "tiles," each consisting of a 3×4 subarray (right). A detailed diagram of a receiver element is also shown (left).

Receivers operate either in the 118-GHz band or the 183-GHz band, controlled by an intermediate-frequency switch. In addition to the large array, which is shared by the two bands, there is a small "low-gain" array (LGA) for each band that fills a gap in the center of the visibility space caused by the large spacings between the receiver feedhorns. The LGA has 39 receivers per arm (117 in total), and the LGAs consist of 3×12 receivers. Spatial resolution is about 25 km at 183 GHz. Mass and power consumption of the full system are small enough that it can be

TABLE I
GeoStorm Performance Specs

Parameter	Specification
Nadir spatial resolution	
118 GHz (temperature)	35 km (0.06°)
183 GHz (humidity)	23 km (0.04°)
Spectral channel specifications	
118 GHz (BW = 300 MHz)	119.2, 119.55, 119.95, 120.35, 120.8, 124.25
183 GHz (BW = 500 MHz)	165.5, 176.31, 180.31, 182.31
Radiometric uncertainty (NEDT) in 15 min	
118 GHz	0.29 K
183 GHz	0.50 K
Instantaneous FOV	1000 km (1.6°)
Targetable FOV	Full Earth disc (nadir±10°)

TABLE II
Some Implementation Options

Option	FOV (km)	T-band (res.)	q-band (res.)	HGAs	Rec's	Size
GeoStorm	1000	118 GHz (35 km)	183 GHz (25 km)	1 HGA 2 LGAs	264	2.5 m
GeoSTAR	5000	118 GHz (35 km)	183 GHz (25 km)	1 HGA 2 LGAs	792	2.5 m
PATH	5000	50 GHz (50 km)	183 GHz (25 km)	2 HGAs 1 LGA	816	4 m

FOV = field of view; T-band = temperature band; q-band = water vapor band; res. = spatial resolution; HGA = high gain array; Rec = receiver.

accommodated as a hosted payload, for example, on a commercial communications satellite. It is intended to be steerable by mounting it on an articulation mechanism, so that the entire Earth disc can be reached.

Table I lists some of the performance specifications of the GeoStorm instrument. The system generates a continuous stream of simultaneous cross-correlations between all receiver pair combinations, cycling through the 10 channels listed in Table I every 90 s, with 11 s dedicated to each of the 118-GHz channels and 6 s to each of the 183-GHz channels. Accumulated correlations are downlinked at the end of each 90-s cycle, and the system can therefore be thought of as providing 90-s sampling of continuous measurements, with each sample representing a 90-s average. The data are typically averaged further in ground processing into longer time intervals, such as the 15-min periods reflected in Table I, to reduce radiometric noise. For some applications, where higher noise can be tolerated, shorter time intervals can be used.

C. Other Implementation Options

The GeoSTAR architecture allows for a number of different implementation options. For example, the FOV can be expanded, spatial resolution can be increased, and different channels sets can be implemented. Table II shows three examples. The "GeoSTAR" option is similar to the "GeoStorm" instrument and has the same overall size, but it has a much larger FOV and is not intended to be steered. The "PATH" option is physically larger and is intended to provide temperature sounding in the legacy 50-GHz band instead of the 118-GHz band. (Its name derives from the 2007 Decadal Survey in that it meets

the measurement requirements of the PATH mission defined there.) Other options not shown could achieve higher spatial resolution (and therefore be physically larger). Note that only the "GeoStorm" option was studied in detail, and the radiometric performance shown in Table I pertain to it.

The GeoStorm architecture in effect implements a "software defined receiving system," since the channel frequencies are defined by an on-board digital synthesizer, which allows channels to be positioned at arbitrary frequencies within broad bands. This makes it possible to achieve in effect hyperspectral sounding, i.e., by rapidly cycling through a number of closely spaced channels, which in turn makes it possible to achieve higher vertical resolution in the boundary layer, for example.

Thus, with the ability to command the set of channel frequencies, the sequence of channels (it is possible to cycle through just the four water vapor channels, for example, to attain higher precision in a shorter time), and the downlink interval (which is baselined at 90 s but can be commanded to a shorter interval, such as 60 s), a wide variety of operational modes and customized data products are possible. A standard set is envisioned that corresponds to the baseline configuration of the instrument and special sets that are requested by users at certain times or for specific applications.

III. Technology

The key technology elements consist of the following (cf. Fig. 5):
1) Correlator subsystem;
2) Local oscillator assembly; and
3) Antenna/receiver building blocks ("tiles")

The correlator subsystem is built up around high-speed low-power application-specific integrated circuits (ASIC).

Here we will only note that all of these elements have been developed and undergone testing in a "relevant environment." Tests included the following.
1) Thermal testing of the correlator subsystem;
2) Radiation testing of the correlator ASIC;
3) Thermal testing of the receiver modules; and
4) Vibration testing of the receiver modules.

A board of experts at JPL has concluded, after reviewing the test results, that the system is at TRL 6, which means that it can be implemented for space.

IV. Simulated Data Products

The sensor data products ["i.e. sensor data records", used by NOAA, or "level 1b" (L1b), used by NASA] that were studied consist of brightness temperatures in the 10 GeoStorm channels, 4 near 183 GHz designed to measure water vapor, and 6 near 118 GHz designed to measure temperature. The specific channel frequencies are listed in Table I, and Table II shows the projected performance in terms of radiometric precision, usually denoted by the "noise-equivalent delta-T" (NEDT) and also called radiometric uncertainty, over a 15-min averaging interval. The instrument's native measurement interval is 90 s, and data are sent to the ground at that rate. There the raw data are converted to visibilities and then to brightness temperatures

and typically averaged over 10 measurement cycles (i.e., 15 min). That results in radiometric precision of about 0.5 K for the water vapor channels and 0.3 K for the temperature channels, as shown in Table I, which is commensurate with the precision attained with current LEO sounders. Corresponding values for the 90-s measurement cycle are about 1.6 and 1 K, respectively. A number of derived geophysical data products [i.e. environmental data record"—EDR used by NOAA, or "level 2"—L2 used by NASA] are then possible. The 15-min radiometric precision is suitable for sounding products (i.e., vertical profiles of temperature and water vapor), while the 90-s precision is suitable for estimating rapidly evolving convective precipitation. Even longer averaging intervals are possible, where the improved precision may be suitable for the study of slowly evolving small signals, such as surface properties.

We note that in a dynamic scene, a certain amount of blurring may occur due to atmospheric motion during the integration interval. For example, if a storm is propagating at 30 km/h, it will move 7.5 km in a 15-min period, which is 30% of the water vapor spatial resolution. If that becomes a concern, a shorter averaging interval can be used, at the cost of increased noise. Such options illustrate the flexibilities offered by the GeoSTAR design.

For the studies discussed below, both L1b and L2 performance was assessed.

A. Simulation Targets (Nature Runs)

A geostationary microwave sounder is of particular value in observing severe weather and storms. Our focus has therefore been on simulated tropical cyclones. Two hurricane case studies were used.

1) Hurricane Harvey: The nature run (NR) used for most of the studies we report consists of a free-running simulation using the Weather Research Forecasting (WRF) model, initialized at 00 UTC 23 August 2017 from the initial state that produced the third strongest member of an ensemble forecast of Hurricane Harvey ([9]; Fig. 6). The NR simulation was run for 5 days (until 00 UTC 28 August 2017), and was driven on the boundaries of the outermost domain by analysis fields obtained from the fifth-generation European Centre for Medium-range Weather Forecasts (ECMWF) reanalysis (ERA5). The NR produces a category 5 hurricane, with minimum sea level pressure less than 920 hPa and maximum 10-m winds in excess of 80 m/s ($>$155 knots). In addition, it rapidly intensifies; during the 24 h between 12 UTC 24 August and 12 UTC 25 August, the minimum sea level pressure decreases by more than 40 hPa and the storm intensity increases from category 1 to category 4. Storm structure on the highest resolution (innermost) domain is highly realistic, both in terms of wind and humidity.

2) Synthetic Hurricane: A second NR was developed by NOAA [10]. That simulation covers a period of 13 days of the life cycle of a fictitious tropical cyclone in the North Atlantic. Fig. 7 shows the track and intensity of the simulated hurricane. It is based on a regional model simulation generated with a WRF nested-grid model running within a global NR generated by ECMWF, called the Joint OSSE global nature run (JONR) in
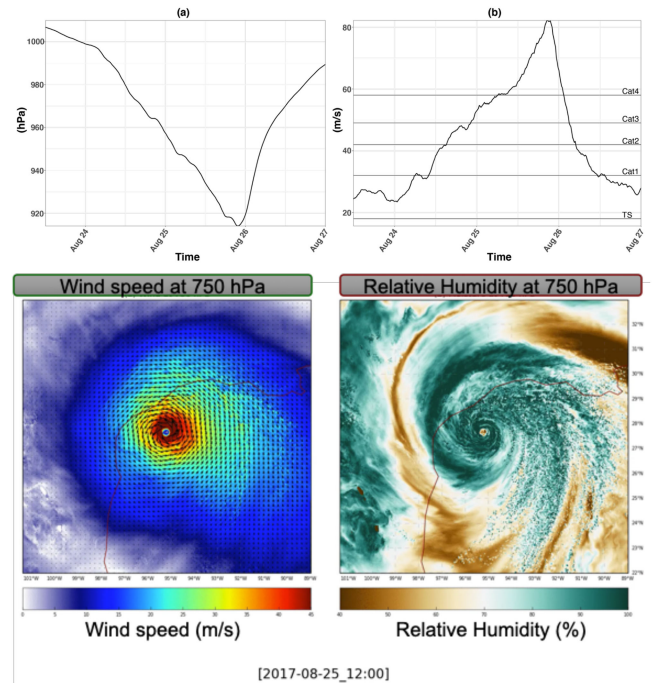

Fig. 6.   Harvey simulation. Upper panel: Minimum sea-level pressure (left), maximum wind speed (right). Lower panel: Output from the NR, valid 1200 UTC 25 August 2017. (Left) Wind speed (color contours) and vectors (arrows) on the 750 hPa pressure level. (Right) Relative humidity (percent; color contours) on the 750 hPa pressure level.
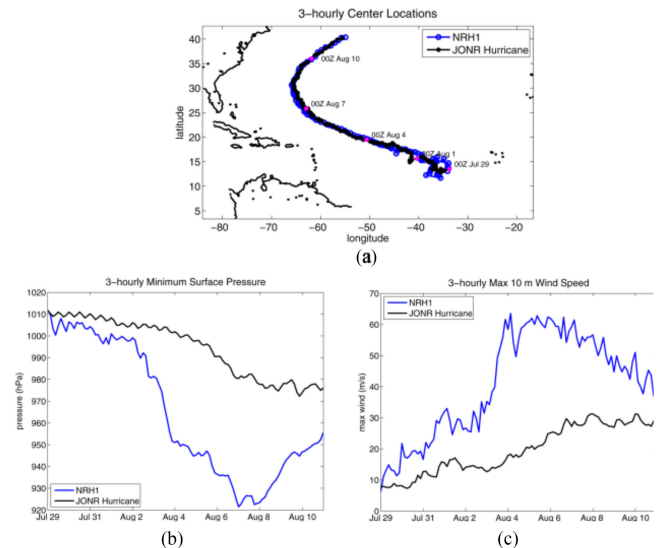

Fig. 7.   Unnamed hurricane (from Ref. [10]). Top panel: Track of the simulated hurricane in the nature run. Lower panels: Min. surface pressure (left) and max. wind speed (right). The global JONR simulations are shown in black, and the regional simulations (used here) are shown in blue.

the figure, where OSSE is a common abbreviation for observing system simulation experiment. The innermost grid has a resolution of 1 km, is sampled every 6 min and covers a 480 km $\times$ 480 km region that is centered on and moves with the cyclone.

B. Brightness Temperature Simulation System

The NASA Earth Observing System Simulators Suite, NEOS[3] [11], is a simulation software system capable of simulating observation products of various satellite-borne instruments such as CloudSat, Cloud-Aerosol Lidar, and Infrared Pathfinder Satellite Observations (CALIPSO), Tropical Rainfall Measurement Mission (TRMM), Global Precipitation Measurement (GPM), and Aerosol Clouds and Ecosystems (ACE), using state-of-the-art techniques and algorithms.

NEOS[3] was developed to be a flexible instrument simulator suite, and its parameters can be reconfigured to target different remote sensing instruments such as radars and microwave radiometers. Fidelity of the simulated products depends on the selection of the microphysics assumptions, electromagnetics, and instrument models. As an example, snow particles may be approximated as spherical ice crystals, which allows quick computation by a Mie scattering algorithm [12] or treated as dendritic particles whose electromagnetics scattering properties are computed based on a more sophisticated algorithm such as DDSCAT [13]. Similarly, several options of wave propagation models have been integrated and are directly selectable by the users. An alternative option, the DS3 [14] model, provides a more accurate simulation, which includes the treatment of multiple-scattering effects. Configurability of NEOS[3] facilitates the study of the impacts of various model assumptions on the final observation.

For this study, NEOS[3] was configured to provide similar capabilities as the Community Radiative Transfer Model (CRTM). Specifically, scattering properties of the ice particles are computed by a Mie scattering model, with the same particle size distribution function that was used to generate the WRF NR (see the preceding section). The background contribution from sea surface scattering is computed by the FASTEM5 model [15], which is also used in CRTM. Finally, the successive orders of interaction [16] radiative transfer model, one of the options that are also supported by CRTM, is utilized to provide the computation of the top-of-atmosphere brightness temperature. Fig. 8 shows the brightness temperature computed for one of the GeoSTAR frequencies from the Harvey NR.

C. Image Processing and Spatial Resolution

One of the characteristics of an instrument that operates in the Fourier domain is that interferometric sidelobes ("ringing") occur when the Fourier spectrum is truncated, as it is here because of the maximum antenna baselines. Fig. 9 shows the GeoStorm point spread function (PSF) and illustrates the hexagonal pattern of sidelobes resulting from the Y-shaped array. Such sidelobes cause image distortions and biases and must be reduced. The conventional approach to suppressing sidelobes is to apply linear apodization, which lowers the sidelobes but leads to loss of information. It also has the undesirable side effect of degrading spatial resolution. Images obtained via this process no longer accurately represent the measurements. Our solution to this problem stems from research in partial differential equation-based image processing that has been made in the last 20–30 years, and also developments in compressed sensing and sparse optimization in
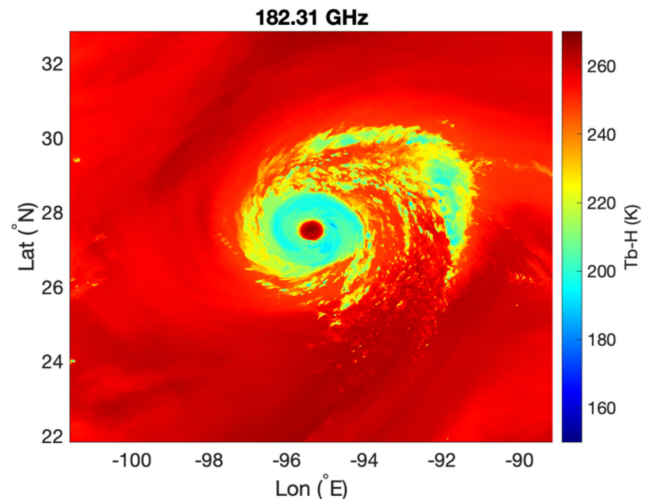

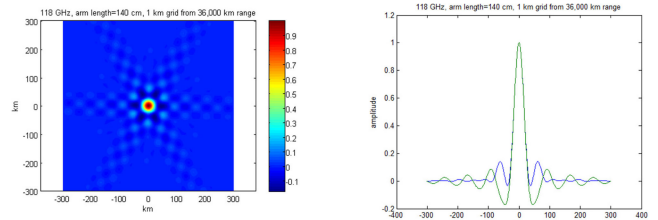Fig. 8.   Simulated brightness temperatures computed with NEOS[3].

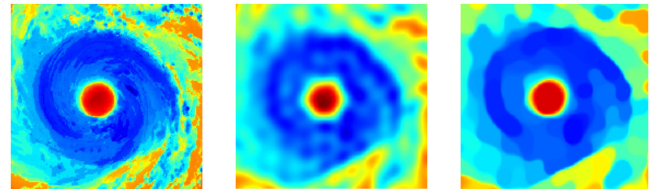Fig. 9.   Point spread function (PSF) of the GeoSTAR instrument.

Fig. 10.   Image processing: WRF image (left), raw GeoSTAR measurement (middle), and reconstructed (right).

the last 10 years. These technologies are now used extensively. In particular, we developed an algorithm using total variation (TV) minimization, and solved it using the split Bregman optimization algorithm [17].

The GeoSTAR PSF, as shown in Fig. 9, is computed accurately from the geometry of the antenna array and channel frequencies, as described by Tanner *et al.* [8]. For our studies, we used NEOS[3] to compute brightness temperature images from the 1-km Harvey WRF simulations, convolved them with the PSFs, and added random noise as shown in Table I, resulting in realistic simulations of raw GeoSTAR brightness temperatures. We then applied the TV technique to remove sidelobe artifacts and recover "clean" images. The results are shown in Fig. 10 for one of the water vapor channels. These images represent a snapshot in time with no motion blurring. Error metrics show a significant reduction of image error in the TV-processed image
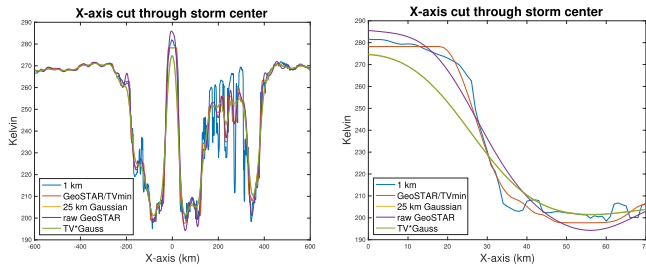
Fig. 11. Image processing performance near the eye wall "edge": Vertical cut through the entire eye (left) and near the center of the eye (right).

compared with the unprocessed one relative to the WRF "truth." It can be seen that the eye in the unprocessed image has a distorted hexagonal shape and is surrounded by artifacts, neither of which appear in the processed image. Edges are preserved.

We also compared with a Gaussian PSF (25-km half-width for 183 GHz and 35-km half-width for 118 GHz), which is considered the ideal PSF for conventional microwave sounders, and found that some metrics showed the TV-method to even outperform the Gaussian. This is illustrated in Fig. 11, which shows a closeup of the eye wall structure. This area has the largest spatial variability and is therefore the most challenging. The figure illustrates that the TV-reconstruction method preserves the sharp edge well and without artifacts and does so better than the Gaussian, i.e., it yields a steeper eyewall closer to the WRF "truth."

Based on these and similar comparisons, we conclude that the GeoSTAR system, after the TV-processing step, has a near-perfect PSF with no remaining sidelobes or artifacts. Due to the nature of the "raw" instrument PSF, with sidelobes showing both positive and negative excursions, it is not possible to compute the conventional beam efficiency metric, but the comparisons with a Gaussian PSF indicate that it is in effect near 100%. Furthermore, we can make the following observations regarding the spatial resolution. A conventional real-aperture microwave sounder, such as AMSU or ATMS, measures the scene through "pixels" that are defined by the half-power width of the main portion of its PSF and which are essentially contiguous and not overlapping (except in the sense that the PSFs overlap). That results in a pixelated image, and the smooth curves shown in the right half of Fig. 11 become step functions, which cannot resolve the fine structure in the eye walls. Therefore, a GeoSTAR with a spatial resolution of 25 km has greater resolving power than a 25-km LEO sounder would. We emphasize that the GeoSTAR sensor produces smooth (but blurred) images and not pixelated images. We also point out that for a real-aperture sounder, the PSF is the same as its FOV, while for an aperture synthesis system, they are entirely different.

D. Simulated Geophysical Products

For some of the studies described below, we simulated the performance of an end-to-end GeoSTAR observing system by approximating the effective transfer functions representing both the instrument and the retrieval system, since it was impractical

to simulate every element separately. The process consisted of convolving the NR geophysical fields with a set of averaging kernels (AKs). Thus, the fields were blurred horizontally with a Gaussian PSF, as discussed above, vertically with representative AKs derived from the retrieval system discussed in the next section, and temporally with a 15-min box-car averaging function. In addition, we added random noise commensurate with the precision metrics also determined from the retrieval system (see below).

V. GEOPHYSICAL RETRIEVAL SYSTEM ASSESSMENT

In summary, an assessment was done in two steps.
1) Simulation of observable brightness temperatures.
2) Use of simulated brightness temperatures in a retrieval system to assess information content and retrieval capabilities.

We assessed the information content by computing AKs and the degrees of freedom (DoF) for temperature and water vapor retrievals. Different channel combinations and noise configurations will result in various DoF, and we statistically compared these by using a variety of atmospheric states. The retrieval capability was tested by running simple retrievals based on the simulated brightness temperatures and then comparing how close the retrievals were to the NR profiles.

To take into account a variety of options for the GeoSTAR configuration, we created two sets of simulations.

A) We created one set of studies to analyze a sizeable observable area in the Northern hemisphere, between 10°W and 120°W longitude and 0°–50°N latitude, with various weather patterns. In this case, we used WRF simulations with a low spatial resolution (25 km) as input to the CRTM radiative transfer model to create brightness temperatures and utilized this information directly in our retrieval system.

B) We created a set of studies focused on observations of an extreme case: the development of Hurricane Harvey. In this case, we used brightness temperatures generated with NEOS[3], which use a different radiative transfer model. The input was the Harvey WRF simulations with a resolution of 1 km. The simulated brightness temperatures from NEOS[3] were convolved with noise and representative spatial response functions (as discussed above) for each channel to create realistic "GeoSTAR-like" observational brightness temperatures, bypassing the imaging processing step described above. We then ran these realistic observations of the brightness temperatures through our retrieval system.

In both cases (A and B), we did the assessment with a JPL in-house retrieval system that uses optimal estimation and offers the capability of calculating AKs and, via them, the DoF.

A. Creating Brightness Temperatures (Tb)

In study A, the low-resolution cases, Tbs were calculated with CRTM from 25-km WRF simulations. Scattering was included and calculated based on rain, ice, and graupel in the WRF simulations. In this case, we used low-resolution 25-km

simulations to cover a wide range of atmospheric conditions, including a tropical cyclone and tropical convection and frontal systems in the mid-latitudes. We put the different atmospheric profiles (temperature, water vapor, liquid water) and surface conditions from WRF into CRTM to convert them into top of the atmosphere (TOA) brightness temperatures. CRTM is capable of calculating scattering impacts from rain, snow, and graupel. It allowed us to calculate these TOA brightness temperatures for all atmospheric conditions.

In study B, we calculated the brightness temperatures similarly but using a different radiative transfer based on the atmospheric composition of high-resolution 1-km WRF simulations. We produced the simulations with NEOS[3] to avoid cross-correlations between simulation and retrieval. The approach is similar: Again, we put different atmospheric profiles (temperature, water vapor, liquid water) and surface conditions from WRF into NEOS[3] to calculate TOA brightness temperatures. However, the radiative transfer approach in NEOS[3] is different from CRTM—circular conclusions are avoided by using a different radiative transfer for simulation and retrieval. NEOS[3] can also incorporate scattering from hydrometeor information to calculate the entire spectrum of precipitation in a tropical storm. Again, in this case, we were using 1-km WRF simulations. To achieve "GeoSTAR-like" observations, the 1-km spatial resolution was then convolved with a spatial response function and white noise to make them realistic observable brightness temperatures from GeoSTAR.

B. Image Processing and Spatial Resolution

"Realistic" brightness temperature observations for the 1-km simulation were achieved by convolving the data and adding noise. The procedure is similar to the methods described in the section on image processing. However, in this case, the method was used to blur the information and try to make it look like after the image processing.

For each channel, the brightness temperature was convolved with the "raw" GeoSTAR point spread function (which has substantial sidelobes) to create a blurred and distorted information content as would be seen from GeoSTAR. Additionally, random noise was added to the observation, again dependent on the channel, but also dependent on the system configuration. TV minimization was then used on this data to eliminate ripples and to create a smooth observation picture as would have been observed by a real GeoSTAR after the image processing.

C. Retrieval System Used for Assessments

The simulated Tbs were used to create geophysical parameters from a retrieval system. The retrieval system is an optimal estimation system that tries to retrieve all constituents at the same time (temperature profile, water vapor profile, liquid and ice water, surface temperature) by minimizing a cost function. The radiative transfer is based on CRTM; noise estimates of the instrument are added via an instrument noise matrix and atmospheric variability is added with a covariance matrix. As with most optimal estimation approaches, the retrievals are underdetermined and therefore dependent on a first guess. In
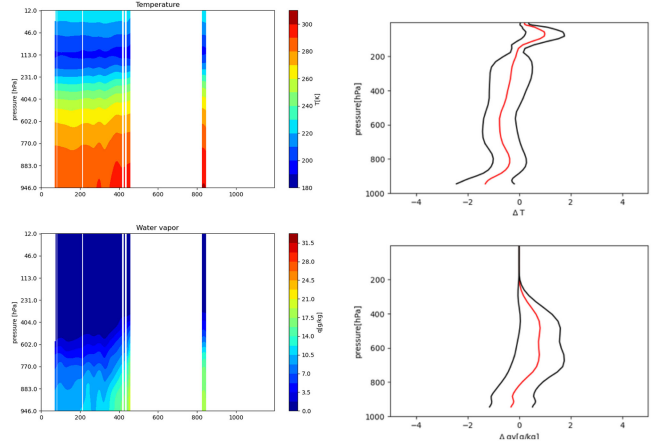

Fig. 12. Cross section of successful retrievals (left) with *high* accuracy and corresponding bias and standard deviation (right).

our case, we tested a variety of first guesses, including model fields from the ECMWF and from WRF, as well as standard atmospheric profiles. However, most results that are shown here are based on retrievals with data from the Modern-Era Retrospective analysis for Research and Applications, Version 2 (MERRA-2) as a first guess, because the system is currently optimized for this approach. We note that MERRA fields are typically available after a month, so they are not suitable for near-real-time applications, but they may still be used in a research context where timeliness is not an issue. We also note that surface properties are treated as fixed and are not solved for in this study. Therefore, results in the boundary layer are overly optimistic.

The success of the retrieval is measured with a convergence criterion that is based on χ^2, computed from the difference between observed and retrieved brightness temperatures.

Dependent on the convergence criteria, we can filter our retrievals and check for usable retrievals. These can then be compared to the NR to estimate bias and error of the retrieval compared to the "real" data. An example for a North–South Harvey cross section is shown in Fig. 12. The left side shows the vertical profiles of temperature (top) and water vapor (bottom) as derived from the retrieval, dependent on the filter criteria of the convergence. The right side shows the bias and rms error when compared to the NR. We note that rms error in the temperature profiles is less than 1 K at all levels, while rms error in the water vapor profiles is less than 1 g/kg at all levels. The latter corresponds to 10–15% in the mid-troposphere. As mentioned above, results in the boundary layer (i.e., 5% rms) should be ignored.

If we use very stringent criteria ($\chi^2 < 1.0$), we can get to within 100 km of the center of the storm (located at point 550 in the figures). The temperature bias is about 1 K, but this is strongly dependent on the *a priori* information.

If we relax the filter criteria and allow weaker convergence, we are able to get even more information. As can be seen in Fig. 13, the information is still usable: Changes in the vertical structure of temperature and water vapor are still apparent, especially
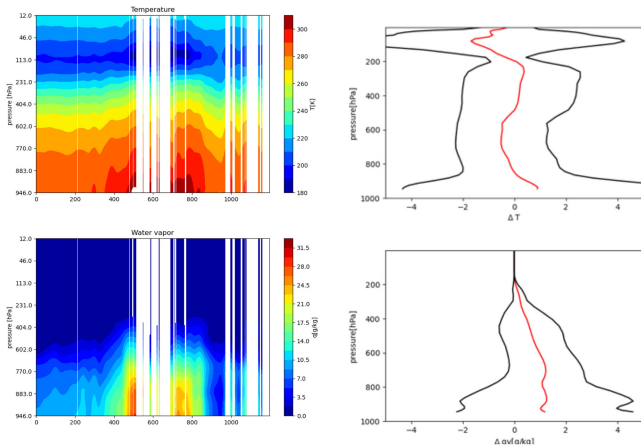
Fig. 13. Cross section of successful retrievals (left) with *good* accuracy and corresponding bias and standard deviation (right).
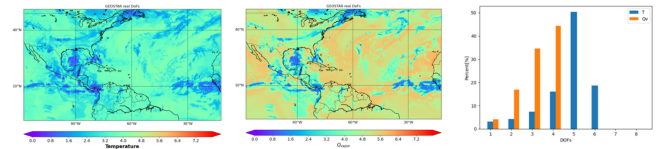

Fig. 14. Degrees of freedom (right) for temperature (left) and water vapor (center) for a wide geographical area surrounding Harvey.
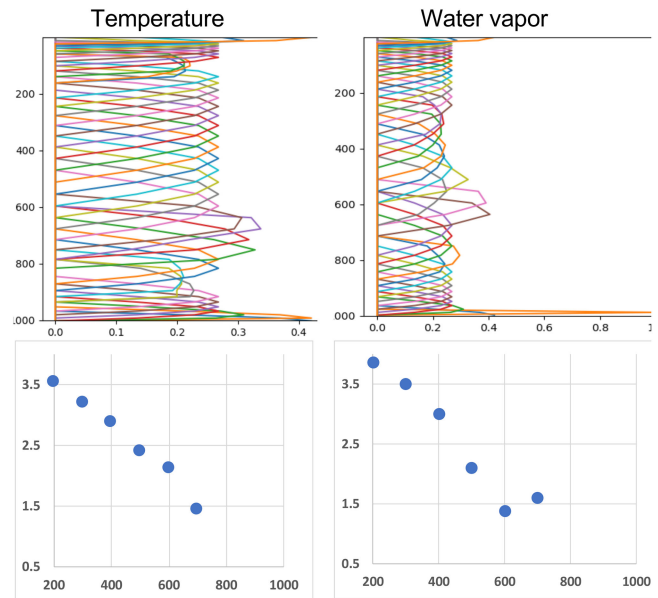

Fig. 15. Averaging kernels (top), vertical resolution (bottom).

when we get closer to the center of the storm. The tradeoff is larger rms errors. Especially in the lower troposphere, we have to deal with a much higher error compared to the stringent filter criteria. However, it becomes also obvious, that we can get close to 50 km from the center of the storm and can even expect some retrievals in the eye.

When we tested the correlation of error and information content, it became very obvious that the amount of precipitation is the main controlling factor. If precipitation increases, retrieval errors increase, even if scattering is included in the calculations.

Another way to assess information content of the system is to determine the DoF of the retrieval. The DoF are calculated by using the diagonal of the AKs for every retrieval point, which allows us to create a map of information content.

D. Information Content Metrics

The main observable variables for a microwave sounder are water vapor and temperature profiles that can be used for assimilation. Other products are surface temperature or rain rate, but that will not be discussed here. The main goal of these simulations was therefore to assess the calculation of information content for the main observable variables. This is done by estimating the DoF for each retrieved variable. The DoF are calculated by using the diagonal of the AKs that can be produced by the retrieval system.

$$\mathbf{AK} = [\mathbf{K}^T\mathbf{S_e}\mathbf{K}][\mathbf{K}^T\mathbf{S_e}\mathbf{K} + \mathbf{S_a}]^{-1}$$

where K are the Jacobians that can be estimated from the radiative transfer. S_e is the estimate for the noise in the instrument, whereas S_a is the estimate for the covariance in the atmospheric information. By calculating the AKs and extracting the diagonals for each variable, we are able to calculate information content of the system.

Fig. 14 shows the results for a simplified study of the 25-km water vapor fields. The calculations were done with the basic GeoStorm configuration: 10 channels (6 around 118 GHz, 4 around 183 GHz) and noise estimates of 0.3 K for 118 GHz and 0.5 K for 183 GHz.

The left side shows the DoF for temperature, the middle for water vapor. The right side shows the statistical distribution. The results depend on a variety of factors, such as overlap of the Jacobians and reliability of the first guess, but it gives a general idea of how much information can be expected from the system, dependent on the atmospheric conditions.

As can be seen very clearly in the figure, the microwave system can cover a wide range of atmospheric states without loss of information. The only factor that impacts the observations is scattering from strong precipitation. For temperature retrievals, this is visible as a drop of DoF from 4 to lower values. In the tropics, they drop in the Gulf of Mexico, where the tropical storm is developing. In the mid-latitude, they drop in the vicinity of frontal systems.

For water vapor retrievals, we achieve more DoF in clear scenes than for temperature. Around 5–6 DoF are apparent in most cases. The reason for drops is again precipitation.

Considering the statistics for this variety of observable states, it is clear that a microwave sounder like GeoSTAR can achieve 3–4 DoF for temperature and 5–6 DoF for water vapor in ∼80% of the atmospheric states. The remaining 20% are precipitating cases, where scattering is impacting our observed brightness temperatures and reducing our capabilities.

Fig. 15 shows the AKs for the areas in Fig. 14 that range from clear to cloudy to light rain (<1 mm/h). Vertical resolution can
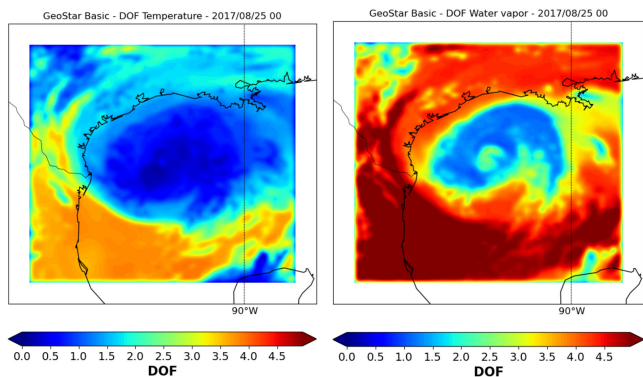
Fig. 16. Closeup of degrees of freedom in the vicinity of Hurricane Harvey.

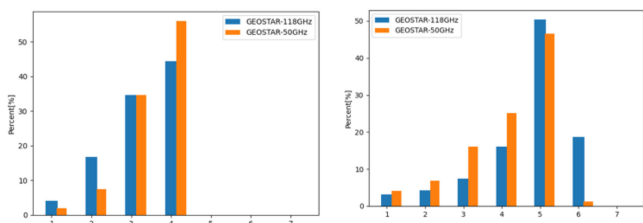Fig. 18. Similar to Fig. 16 but using 50-GHz channels instead of 118-GHz.

Fig. 17. Comparison of DOF distributions for 50 GHz (orange color) vs. 118 GHz (blue color); for temperature (left) and water vapor (right), using simulated data.

be estimated from the widths of the AKs, and the results are also shown. Vertical resolution for temperature ranges from 1.5 km in the lower troposphere to 3.5

Fig. 16 shows the DoF for a range of ~1000 km around Hurricane Harvey, which approximates the observations that would be obtained with the "GeoStorm" implementation if it were pointed at the center of the hurricane. There is high information content south of the storm for temperature, but it drops significantly closer to the center of the storm. Water vapor, on the other hand, can provide high information content in ~60% of the area, even in the center of the storm. Only strong precipitating areas are affected by a drop in information content.

E. Sounding Performance of 118 GHz vs. 50 GHz

One of the questions with respect to instrument design is the impact of 118 GHz for temperature sounding in comparison to legacy channels near 50 GHz. 118 GHz is easier to implement from an engineering perspective, but channels around 50 GHz have a legacy in microwave sounding. From the retrieval perspective, 50-GHz channels have both advantages and disadvantages.

The statistics in Fig. 17 are taken from the analysis with low spatial resolution. If we replace the 118 GHz with similar channels around 50 GHz (i.e., with the same nominal weighting functions), we get a slight advantage in temperature sounding. There are obviously more areas with high DoF. On average, the amount of 4 DoF is increased by around 10%. The information content in the water vapor analysis, on the other hand, is dropping, and the areas with 6 DoF drop from 18% to 3%.
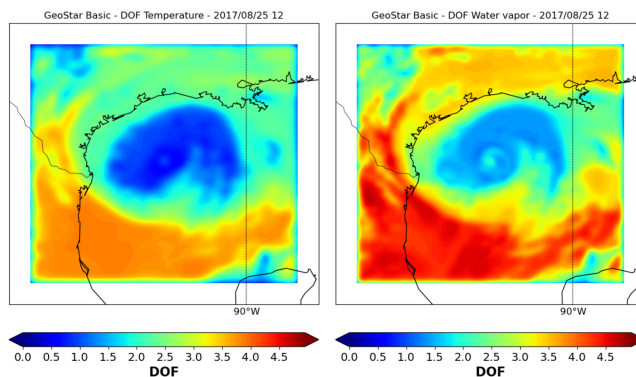
The reason for this behavior becomes clearer if we compare the results from the targeted observation of hurricane Harvey by comparing Fig. 16 (118 GHz configuration) with Fig. 18 (50 GHz) configuration.

In areas with high precipitation, the 50-GHz channels are less prone to scattering impacts and can therefore produce more information content. 118 GHz channels have a shorter wavelength and are therefore more impacted by hydrometeors. The temperature information content is therefore higher for 50 GHz channels, if strong precipitation is involved. The higher information content is matched by lower spatial resolution and more blurring, however. The simulations at 50 GHz show lower fine-scale structure and smoother temperature fields than at 118 GHz.

Another effect is the impact on the water vapor information. If we replace 118 GHz with 50 GHz, we can observe a drop in DoF for water vapor. The impact is due to a drop of information content in the water vapor continuum, which is slightly better at 118 GHz Also, the Jacobians show that the vertical information content of 50 and 183 GHz overlaps a little bit more than the Jacobians of 118 and 183 GHz. The advantage of a reduced scattering impact at 50 GHz is therefore mitigated by a reduction of water vapor information. Both approaches have therefore advantages and disadvantages with respect to information content. The technical considerations, however, would favor a 118-GHz approach.

To verify this difference under realistic observations, we applied the same test to real observations. To achive this, we used airborne observations from the High-Altitude MMIC Sounding Radiometer (HAMSR), an airborne microwave sounder with matching channels in both bands. During a campaign in 2017, it flew over the actual Hurricane Harvey while it was undergoing reintensification in the Gulf of Mexico. HAMSR has a set of 118-GHz channels and a set of 50-GHz channels, together with a set of 183-GHz channels. We selected an overflight of the eye witihn a timeframe of 1 h and analyzed the DoF statistics.

Fig. 19 shows the results. The left plot shows the DoF for temperature, and the right one for water vapor. As can be seen, in both cases, the 50/118/183 GHz (green) has the highest success rate. Orange statistics show a retrieval without 118 GHz and blue is without 50 GHz. With respect to temperature, the 50-GHz
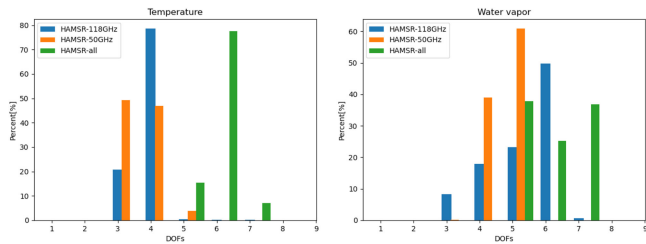
Fig. 19. Comparison of DOF distributions for 50 GHz (orange color) vs. 118 GHz (blue color); for temperature (left) and water vapor (right) using HAMSR data.

Fig. 20. DoF statistics when adding a transparent 183-GHz channel, for temperature (left) and water vapor (right).

approach achieves a few better observations with 5 DoF, but not many. And considering DoF values of 3 and 4, it seems to provide less information than the 118-GHz band. For water vapor (right panel), 118 GHz can provide more information in many cases: 50% provide 6 DoF. However, it should also be mentioned that the 50-GHz band seems to provide more stable information, with 3 and 4 DoF under most conditions.

HAMSR's error characteristics are slightly different than GeoSTAR's, but overall, real observations confirm the results from simulations. Statistically, 50 GHz has slight advantages with respect to temperature sounding; 118 GHz, on the other hand, can provide more water vapor information. The overall performance is very dependent on the individual scene.

F. Performance With Additional Sounding Channels

The implementation of 50 GHz instead of 118 GHz—or both—is significantly more difficult from a technical point of view. However, a relatively "easy" way to change the performance of the instrument is to add channels within the given configuration. The basic 118/183 GHz configuration has 10 channels. But the instrument can sample a range of frequencies, since the channel set is defined by an on-board table of frequencies for the synthesizer that drives the local oscillator. Therefore, it is feasible to add channels to the baseline configuration. The main caveat is that adding channels to the basic configuration increases the noise in each channel, since there is less integration tme available to each channel. So, if we add channels, we have to add noise in our simulations. We simulated this approach by adding a water vapor channel at 173 GHz. This channel would be more sensitive to lower level water vapor information. To keep it realistic, we also increased the noise for channels around 118GHz to 0.3 K and around 183 GHz to 0.6 K. However, the statistical information content in Fig. 20 shows that the impact of the noise is outweighed by the increase of information content: By adding a channel at 183-10 GHz (173 GHz), we achieve a slight increase in information content for temperature. DoF are not getting higher than 4, but the amount of 4 DoF is increasing by 8%. For water vapor, the entire distribution is shifted: We have now areas with up to 7 DoF, even if the area is only 3% of all cases. The areas with 6 DoF, however, are increased drastically: from 18% to 58%. Adding one channel, therefore, results in significantly more cases with higher information content.
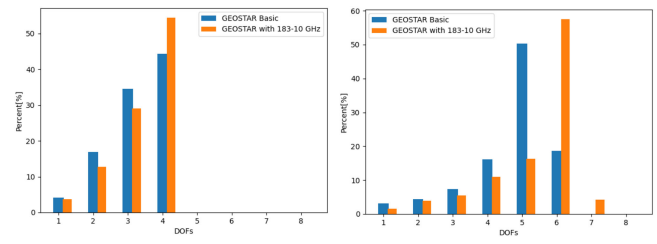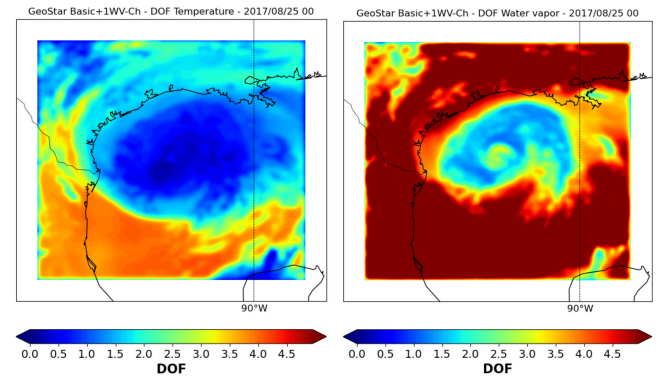

Fig. 21. DoF spatial distribution when adding a transparent 183-GHz channel, for temperature (left) and water vapor (right).

This is also the case for extreme weather conditions, as is shown in the targeted observation of Hurricane Harvey, seen in Fig. 21. As can be seen, the information content for temperature sounding is slightly increased, especially in areas where we had only 1 or 2 DoF before. But more significantly, the water vapor sounding is enhanced drastically. The areas with more than 5 DoF covers most of the observed area, and the eye of the storm is clealry visible with ∼3 DoF. Only for strong precipitating areas do we see a drop in information content.

Overall, the use of additional channels within the basic configuration seems to be a simple way to add information. Statistically, it can provide significantly more information about water vapor. The replacement/addition of 50 GHz to the system can help to achieve a slighlty better temperature sounding under scattering conditions. However, this is technically much more complicated than adding channels to the basic configuration range.

We note that the DoF we report here equal or exceed those of a modern IR-MW sounder retrieval system, the Community Long-Term Infrared Microwave Combined Atmospheric Product System (CLIMCAPS), as reported by Smith and Barnet [18], who found DOF up to 3.5 in the tropics.

VI. 3-D WIND PRODUCT ASSESSMENT

We have previously carried out simulations to demonstrate the capability of obtaining wind vectors using the atmospheric motion vector (AMV) method of tracking the motion of water vapor [19]. Realistic atmospheric conditions were represented by a hurricane NR, and simulated observations were derived
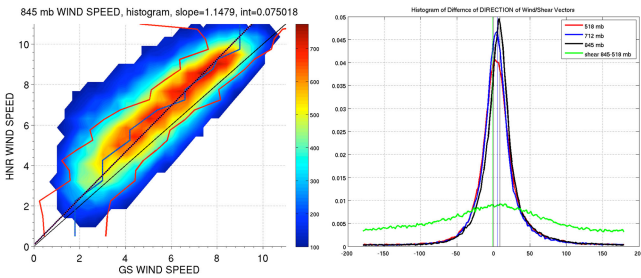
Fig. 22. Histograms of simulated AMV wind retrievals. Left: wind speed in m/s ("GS" = GeoSTAR, horizontal axis) vs. nature run "truth" (vertical axis) at 845 hPa. Right: wind direction errors in ° (horizontal axis) at three different pressure levels; the green curve is for wind shear (here defined as the difference between 845 and 518 hPa). From Ref. [19].

from the NR. The results are summarized here for the reader's convenience.

The simulations were based on an NR generated for NOAA, as discussed above ("synthetic hurricane," Section IV-A.2). The simulations cover a period of 13 days of the life cycle of a tropical cyclone.

We used the method discussed in Section IV-D to generate realistic and representative water vapor fields, which are used by the wind algorithm. Here we will just summarize by saying that we blurred the 1-km 6-min WRF fields horizontally with a 25-km Gaussian kernel, vertically with a blurring function derived from the retrieval system (see Section V-D) that corresponds to a 2–3-km vertical resolution, and temporally with a 15-min box-car kernel. In addition, rain estimates produced by the WRF simulations were used to mask out all cases where the rain rate exceeded 3 mm/h but allow water vapor profiles between the surface and 700 mb when the rain rate is between 1 and 3 mm/h and accept all profiles when the rain rate is 1 mm/h or less. Based on recent advances in retrieval techniques discussed above, we expect actual performance will exceed those limits, and our results are therefore conservative estimates.

Fig. 22 shows a two-dimensional histogram of wind speed derived from the GeoSTAR simulations (horizontal axis) vs. the NR model "truth" (vertical axis) at one pressure level, and histograms of wind direction errors at several pressure levels. In the wind speed plot, color indicates data point density, and the red lines denote the 1-sigma levels. The black line represents a linear fit, and the numbers above the plot are the linear-fit parameters. Outliers (e.g., large true wind speeds but low retrieved wind speeds) are caused by AMV algorithm errors associated with large displacement and feature distortion and by sparse sampling in these mostly precipitating areas. We expect that a shorter sampling interval (which is feasible with GeoSTAR, as discussed in the instrument section) will make it possible to accurately retrieve these high wind speeds as well. The number of cases is quite low and can also be flagged with appropriate quality control and is therefore not of concern. The reader is referred to Ref. [19] for further details, where results over a much wider dynamic range are shown.

In the histogram of wind direction errors, the half-widths of the distributions range from 24° (845 hPa) to 32° (518

TABLE III
SIMULATION RESULTS (WIND SPEED AT 6 M/S)

Pressure level (mb)	Bias		RMS error	
518	-0.8 m/s	2°	1.9 m/s	14°
712	-1.2 m/s	3°	1.6 m/s	11°
845	-1.0 m/s	6°	1.7 m/s	10°

From Ref. [19].

hPa), corresponding to rms errors ranging from 10° to 14°. It can therefore be stated that wind direction is retrieved with a precision of ±15° or better, except for shear. The latter, which is only computed at a given location when wind vectors at both 845 and 518 hPa can be determined, shows relatively poor precision, which is likely because it is difficult to achieve precise matches between the three temporal snapshots required by the AMV algorithm in a dynamic environment with variable gaps due to precipitation. We surmise that much better results would be obtained by differencing wind vector images where gaps can be filled.

We note that the results are largely insensitive to noise, i.e., the results we achieved with noise (25% random noise added to water vapor profiles) and without were indistinguishable. This is because the effective noise within the 32×32 search box is reduced by a factor of 32. Retrieval errors are therefore dominated by AMV algorithm errors and the direction and magnitude of gradients and variability in the moisture fields.

Table III summarizes the results for three pressure levels. Bias near the peak of the distributions ($\sim$6 m/s) is about -1 m/s, and the RMS error is less than the 3 m/s WMO "breakthrough" requirement for tropospheric wind speed.[1] The bias, which is small compared with results derived from cloud tracking, may be caused by the effective spatial averaging inherent in the AMV algorithm, while the "truth" represents a point value in the center of the averaging box. This has not been fully explored.

VII. HURRICANE INTENSITY

Scientists at the Cooperative Institute of for Meteorological Satellite Studies (CIMSS) at the University of Wisconsin have developed a method to use low-earth-orbiting microwave sounders to estimate the intensity of tropical cyclones [20]. The method is based on strong correlation between the strength of the warm core of a TC and the surface pressure anomaly in the eye. An algorithm was developed that uses the brightness temperatures of AMSU channels that have peak sensitivity in the upper troposphere, as shown in Fig. 23. The warm core anomaly typically peaks near 250 mb, and the AMSU channel 7, which has peak sensitivity there, is the most important. Its center frequency is at 54.94 GHz.

GeoSTAR has channels in the 118-GHz band with weighting functions nearly identical to those of AMSU, and in particular, the channel located at 119.55 GHz peaks at 250 hPa as does AMSU channel 7. We used the NOAA NR used in the AMV study discussed above.

---

[1][Online]. Available: https://www.wmo-sat.info/oscar/requirements/view/313
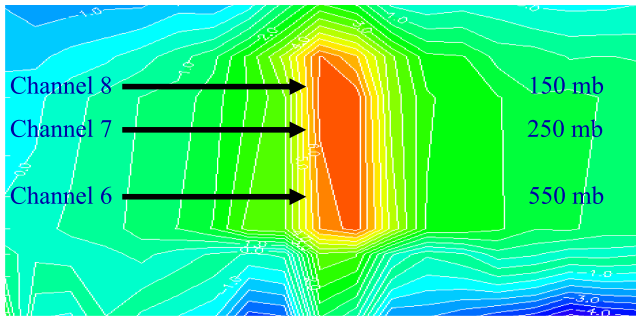
Fig. 23. Typical TC warm core anomaly and AMSU channels 6-8. From Ref. [20].
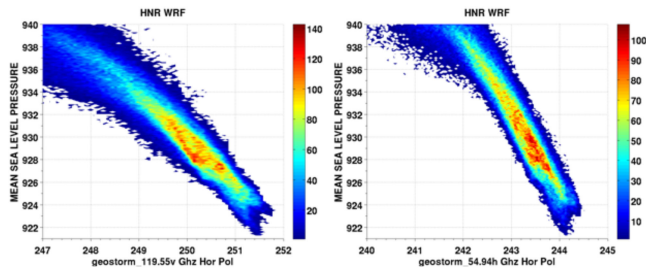

Fig. 24. Simulated TC intensity: Min. pressure (vertical) vs. Tb (horizontal). GeoStorm 119.55 GHz (left), AMSU 54.94 GHz (right).

The data set used is described in the AMV wind vector section above. The results are shown in Fig. 24, which shows mean sea level pressure (MSLP) vs. brightness temperature computed from the WRF simulations (hurricane NR, HNR) for the GeoSTAR 119.55-GHz channel (left panel) and the AMSU 54.94-GHz channel (right panel) for a large number of samples corresponding to Category 4. It can be seen that there is a near-linear relationship in both cases. The sensitivity of the GeoSTAR channel is approximately 0.25 K/hPa, which is nearly twice that of the AMSU channel, 0.14 K/hPa. With an NEDT of better than 0.3 K with 15-min averaging, we project an MSLP retrieval precision of 1.2 hPa in this range, compared with 1.8 hPa for AMSU. CIMSS reports [20] an RMS of 6.3 hPa, which includes errors related to misalignment between the AMSU FOV and the center of the hurricane, a problem that does not exist for GeoSTAR. There are other error sources, such as Tb depression due to scattering in the eye walls, which is related to the size of the inner core. In summary, we expect GeoSTAR to outperform AMSU in this area. With its continuous measurements, GeoSTAR will be able to provide intensity estimates both more frequently and more accurately than can currently be done.

We conclude that real-time estimates of TC intensity can be derived from GeoSTAR with excellent accuracy as well as very rapidly and in real time. In the next section we show that the prediction of Harvey benefits from assimilation of the MSLP estimates derived from the 119.55-GHz channel. A more advanced (and more accurate) algorithm would use information from additional channels, similar to the CIMSS method. We note that the capability of estimating hurricane intensity from MW sounder observations already exists and is used operationally;

this can only be done when the satellite passes in the vicinity, i.e., at best every 12 h and usually at much longer intervals. With GeoSTAR, it will be possible to monitor the intensity continuously, which is crucial for the ability to detect rapid intensification, rapidly forming eye wall replacement cycles, diurnal modulation of intensity, and other rapid phenomena that are important for accurate forecasting.

VIII. OBSERVING SYSTEM SIMULATION EXPERIMENTS (OSSE)

In addition to the synthetic retrieval experiments described above, we conducted experiments to assess the potential impact of assimilating geostationary microwave soundings on numerical weather prediction forecasts. We chose for our analysis the tropical cyclone case described in Section IV-A that is very similar to hurricane Harvey (2017), as hurricanes are among the most devastating of weather-related natural disasters, and hurricane intensity continues to pose a significant challenge for numerical weather prediction. It is hypothesized that better characterization of the hurricane environment, especially before and during intensification, may lead to significant improvements in forecasts of hurricane track and intensity. In this regard, we anticipate that assimilation of the high spatial and temporal resolution soundings from the GEO MW instrument may have a strong positive influence on tropical cyclone weather prediction. The OSSEs are described in detail in a separate paper [21], and here we will only summarize the results for a series of regional OSSEs. (Global OSSEs were also run, and the reader is referred to the full OSSE paper for that aspect.)

The NR in our OSSE consists of a free-running simulation using the WRF model, initialized at 00 UTC 23 August 2017 from the initial state that produced the third strongest member of an ensemble forecast of Hurricane Harvey. The NR simulation is run for 5 days (until 00 UTC 28 August 2017), and is driven on the boundaries of the outermost domain by analysis fields obtained from ERA5 reanalysis. The NR produces a category 5 hurricane, with minimum sea level pressure less than 920 hPa and maximum 10-m winds in excess of 80 m/s (>155 knots). In addition, it rapidly intensifies; during the 24 h between 12 UTC 24 August and 12 UTC 25 August, the minimum sea-level pressure decreases by more than 40 hPa and the storm intensity increases from category 1 to category 4. Storm structure on the highest resolution (innermost) domain is highly realistic, both in terms of wind and humidity.

We utilized an older version of the WRF model, run on a different (coarser resolution) domain and with different physical parameterizations and boundary conditions, as our forecast and assimilating model. An ensemble Kalman filter (EnKF) was used to assimilate conventional data and GeoSTAR profiles. We utilized the same conventional dataset as has been used in previous studies (surface METARs, ship observations, radiosondes, and satellite winds), but rather than using real observations, we instead simulated observations from the NR by extracting data from locations identical to the real measurements and then applying uncertainties consistent with real observations.

We utilized a 60-member ensemble for the EnKF, and initialized from an initial state obtained from the NCEP FNL analysis

Pressure (hPa)	Temperature (K)	RH (%)	Wind (m/s)
1000	2.2	14.0	2.0
850	1.6	15.0	2.0
700	1.4	16.0	2.0
600	1.4	16.0	2.0
450	1.4	16.0	2.0
300	1.4	18.0	2.0

valid at 00 UTC 23 August 2017. The initial ensemble was generated using the WRF data assimilation system's RANDOMCV methodology, which applies random perturbations to the model initial conditions in control variable space.

In our experiments, we blurred the NR temperature and water vapor profiles horizontally and vertically, as described above. In addition, we selected discrete layers for assimilation based on the information content analysis in the retrieval system, and with layer locations equal to the peaks in the retrieval AKs. The specific vertical levels assimilated are (850, 700, 600, 450, 300 hPa) and the uncertainties in temperature and relative humidity are listed in Table IV. Assimilation of temperature and water vapor profiles forms the basis for nearly all of our OSSEs; however, we also ran two additional experiments; one in which we assimilated wind vectors (assumed to be obtained by tracking retrieved water vapor), and another in which we assimilated a GEO MW-based estimate of the TC minimum central pressure using the algorithm described in Section VII.

A. Description of the Assimilation Experiments

1) Baseline Experiments: As a baseline, we ran two experiments that did not assimilate synthetic GEO MW temperature and water vapor profiles; one in which no observations are assimilated (NoDA), and another in which only "conventional data" were assimilated (Conv or Conventional), also called the control experiment. Conv is meant to replicate the results that would be obtained when all currently available observations are assimilated, including surface, radiosonde, aircraft, and the current set of satellite remote sensing measurements. In our regional OSSEs, the domain was nearly entirely over the Gulf of Mexico during the assimilation time period. Because of the regional domain and intermittent overpass times and large latency times of low-earth-orbiting satellites, we did not assimilate any current LEO satellite data. We did incorporate data from ships, surface METARS (where available), and any radiosondes in the domain. We also assimilated synthetic geostationary wind (AMV) data (SATWIND). No hyperspectral IR data were assimilated.

2) Geostationary MW Experiments: As mentioned above, the majority of our experiments assimilated temperature and water vapor profiles consistent with GeoSTAR retrievals. In contrast to infrared sounders, microwave sounders are able to retrieve profiles in cloudy regions (though the presence of precipitation increases the retrieval uncertainty). To analyze the effect of assimilating information in cloudy and precipitating regions, we conducted the following experiments.

1) Only assimilate profiles in clear-sky regions—those with broadband outgoing longwave radiation $>220 \, \text{W/m}^2$. This effectively screens out all clouds above the boundary layer.
2) Assimilate all clear-sky profiles as in (1), and add profiles in cloudy regions with precipitation rates up to 1 mm/h. Consistent with the results returned by the retrieval system, the uncertainties in cloudy and lightly precipitating regions are expected to be the same as those for cloud-free profiles.
3) Assimilate clear sky profiles as in (1), and add profiles in cloud regions with precipitation rates up to 10 mm/h. This is the maximum rain rate under which we expect to be able to retrieve temperature and water vapor. To account for increasing error in the retrievals,
4) we inflate the assumed uncertainty in the observations according to precipitation rate, with $0.1–1.0 \, \text{mm/h} = 2\times$ uncertainty, $1.0–10 \, \text{mm/h} = 3\times$ uncertainty.

As mentioned above, we also ran two additional experiments.

5) As in (2) above, but also assimilate synthetic geostationary AMVs. These consist of winds obtained from the NR, blurred to the GeoSTAR horizontal and vertical resolution, and then thinned to 100 km horizontal spacing. Errors are listed in Table IV.
6) As in (2) above, but also assimilate estimates of the tropical cyclone central pressure obtained from the GeoSTAR-estimated TC warm core thermal perturbation. Uncertainties on the minimum SLP estimates were conservatively set to 11.9 hPa.

Experiments (1)–(5) assimilated GeoSTAR data hourly. We also conducted a sixth experiment, in which experiment (2) is repeated with 15-min update intervals. This is the highest frequency with which we can retrieve temperature and water vapor and maintain the expected uncertainties and horizontal resolution.

B. Results

1) TC Intensity: Results from a control forecast, as well as a forecast that assimilates conventional data, showed that neither is able to successfully capture the NR hurricane development. In contrast, assimilation of GEO MW soundings from all three configurations resulted in demonstrable improvement, with the clear-sky-only experiment producing a relatively weaker storm compared with assimilation of all-sky profiles with and without precipitation dependent error. The most realistic (strongest) storm was produced from assimilation of 15-min interval GEO MW data, with the storm reaching strong category 4 intensity and with intensification rates very similar to the NR. As an example, Fig. 25 shows the results when wind vectors are assimilated along with the thermodynamic profiles. Further details can be found in Ref. [21].

2) TC Track Error: Another metric commonly used to assess tropical cyclone forecast accuracy is the track position of the center of the storm, commonly represented as a deviation (or error) from the reference (or Best Track) position. In our case, we have exact knowledge of the storm center position from the NR, and compute hourly great circle distances between the NR
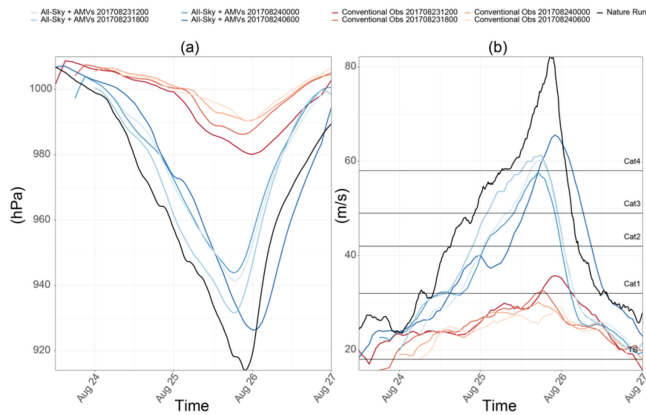
Fig. 25. Min. pressure (left) and max. wind (right). Warm colors: assimilation of conventional data; cool colors: assimilation of GeoSTAR data (temperature, RH and wind with precipitation <1 mm/h); light colors: earlier initialization times; dark colors: later initialization times; black is the nature run. From [21].
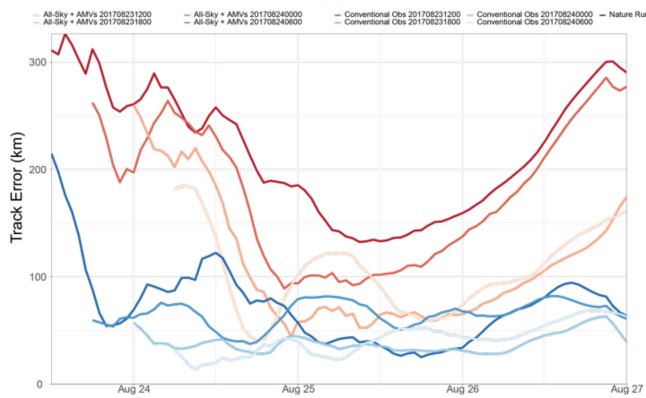

Fig. 26. Forecast track errors for the cases shown in Fig. 25, using the same color scheme. From Ref. [21].

TC center and the TC center in each of our data assimilation experiments. Plots of the track error are shown in Fig. 26 for the experiment with wind vector assimilation, and it can be seen that track errors in the experiment with conventional data assimilated (warm colors in each plot) are on the order of 50–300 km. Assimilation of Geo MW data has a similar effect on track for all configurations tested, with track errors smallest for experiments that assimilated AMVs in addition to temperature and water vapor profiles.

3) Storm Vertical Structure: In addition to metrics of storm intensity, it is also useful to examine the storm vertical structure. Two common measures are the temperature deviation from the mean, which reveals the positive temperature perturbation in the storm's inner core, and the u-direction (east–west) component of the wind, which reveals the storm's overturning circulation. We have computed both of these metrics for the NR, control simulation, and each of the Geo MW experiments.

Examination of the temperature perturbation reveals a strong positive thermal anomaly in the upper troposphere in the NR, consistent with observations of strong tropical cyclones. 00 UTC 26 August is near the time of peak intensity, and as

such the perturbation is deep and strong. A weaker negative perturbation is evident near the surface, consistent with low-level cooling due to evaporating precipitation. By comparison, while the conventional assimilation experiment does produce a warm core anomaly, it is relatively weak and peaks at a lower level. In addition, the near-surface negative temperature perturbation is more widespread, extending to greater than 300 km from the storm center. Assimilation of GEO MW profiles results in improvements to storm structure in all cases, though the 15-min assimilation cadence appears to produce the storm structure that best matches the NR.

The NR zonal mean winds exhibit a deep region of strong winds extending from near the storm center to a radius of 100 km, with weak winds aloft, reflecting the presence of upper level outflow. Consistent with the thermal perturbations, the conventional experiment's winds are too weak, and do not extend high enough into the troposphere. Each GEO MW assimilation experiment produces improved wind structure, with the 15-min assimilation cadence case, and the case in which TC central pressure is assimilated, producing the most realistic winds.

4) Effect on the Storm Environment: In addition to the effect of assimilating GEO MW profiles on the tropical cyclone characteristics, we also wish to know whether profile assimilation resulted in improvements in the storm environment. We measure this by computing the root-mean-squared error (RMSE) for the mean profiles of temperature, water vapor, and wind between each forecast experiment and the NR. To ensure consistency, we compute RMSE between the forecast and the 3-km resolution NR domain (domain 03), and reduce the size of the NR domain to match the forecast domain. The outcomes are quite similar for all GEO MW assimilation experiments; hence, we show only the results from the all-sky GEO MW assimilation experiment in which precipitation rates are limited to <1 mm/h.

We found that GEO MW data assimilation results in small improvements to environmental temperature, and a slight degradation in water vapor. The most notable improvement is to the environmental winds, for which the RMSE decreases by more than 50%. Analysis of the mean vertical profiles of RMSE over the same time period reveals that the temperature improvements are maximized in the lower and upper troposphere, with a slight degradation in the middle troposphere (400–600 hPa), and that these improvements are not statistically significant. Specific humidity improvements are concentrated in the lower to middle free troposphere (~700 hPa) with small (but statistically significant) degradations near the surface and in the upper troposphere. Wind improvements are largest in the middle and upper troposphere between 750 and 250 hPa, with a decrease of 50% for zonal wind RMSE and 72% for meridional wind RMSE.

While the storm structure and intensity are improved by assimilation of GeoSTAR profiles, there are small, but statistically significant, degradations in the representation of the specific humidity. It is possible that the coarser resolution representation of convection in the assimilating model resulted in errors in the vertical transport of water vapor, but additional analysis would be needed to determine the specific processes involved.
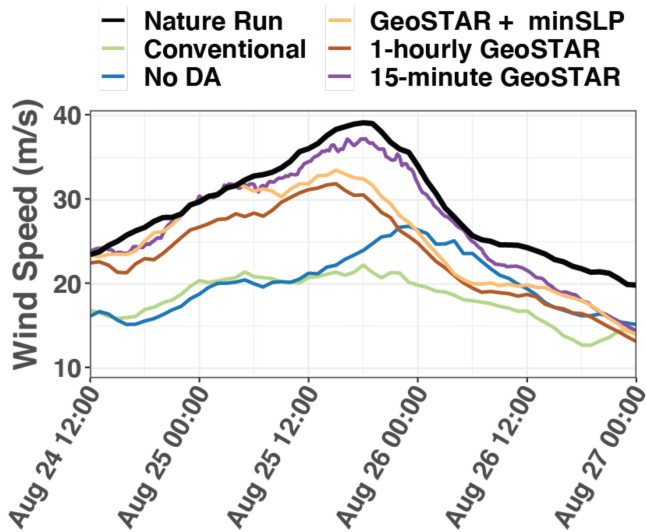
Fig. 27. Time series plot of the 99th percentile of the near-surface wind speeds in the nature run (black), no-DA experiment (blue), control experiment (green), GeoSTAR with (yellow) and without (red) minSLP assimilation, and GeoSTAR 15-min assimilation frequency (purple). From Ref. [21].

5) Surface Wind Speed Statistics: Examination of the wind extremes (Fig. 27) reveals that the no-DA and conventional assimilation experiment (which is referred to as the "control experiment" in the caption of Fig. 27) are unable to reproduce the strong winds in the storm, especially at early times (prior to 00 UTC 26 Aug). Assimilation of GEO MW data improves the wind speed statistics, with 15-min assimilation yielding a very close match to the NR wind extremes through most of the storm's evolution.

6) Final Remarks: There are a few caveats that should be kept in mind when interpreting the results of this study. First, effective data assimilation of a new set of observations requires an extensive period of observation tuning and calibration during which time optimal channels are selected and forward model errors are mitigated. In addition, assimilation of synthetic retrievals is not the norm in modern data assimilation; rather, most operational centers prefer to ingest radiances and use the forward operators in the data assimilation system to convert back and forth from the model state variables. The short duration of this study precluded us from 1) tuning the retrieval system and AKs, 2) producing a set of synthetic retrievals for assimilation (e.g., by forward simulating radiances from the NR, then running these radiances through the GEO MW retrieval to produce synthetic temperature and water vapor profiles), or 3) making the modifications necessary to the data assimilation system to ingest radiances (and select channels). We expect that, should future GEO MW observations be available, the operational centers would choose to assimilate radiances from a carefully chosen, calibrated, and debiased selection of channels.

IX. CONCLUSION

The simulation studies discussed here present strong evidence that a geostationary microwave sounder can provide a number of important measurements of atmospheric parameters, ranging from temperature and water vapor to vertical profiles of horizontal wind vectors, with high precision, accuracy, and coverage. In particular, with the ability of a sounder to achieve absolute height registration and the ability of microwave sounders to penetrate clouds, it will be possible to make these measurements almost everywhere. Only precipitating areas will result in gaps, and even there one can expect evolving retrieval technology to soon fill such gaps as well. In addition, our studies indicate that such measurements will lead to significant improvements in hurricane forecasting, and by extension to severe weather in general. Here is a concise summary of our findings.

1) A geostationary microwave sounder is now feasible.
2) The GeoSTAR instrument achieves performance from GEO that matches or exceeds the performance of current LEO sounders. (Performance estimates are based on simulations in/around hurricanes)
   a) Temperature profiles with a precision better than 1 K.
   b) Water vapor profiles with a precision of about 10%
   c) Vertical resolution of 1–2 km.
   d) Horizontal resolution of 25 km for water vapor and 35 km for temperature.
   e) Updates every 15 min or better.
      a) As fast as every 90 s, suitable for high-intensity precipitation.
   f) Uniquely: atmospheric "AMV" wind vectors, under all conditions, including in and below clouds, with an accuracy exceeding WMO requirements.
   g) OSSE studies show significant impact on regional and global forecasts.
      a) With a simulated Cat5 hurricane, modeled on Harvey (2017), assimilation of GeoSTAR data produced a strong Cat4 storm while conventional data did not reach Cat1; GeoSTAR-derived wind vectors and minimum pressure were particularly impactful.
   h) Continuous operation enables real-time weather surveillance.
3) The underlying instrument performance equals or exceeds current LEO sounders.
   a) Six temperature sounding channels with NEDT = 0.3 K.
   b) Four water vapor sounding channels with NEDT = 0.5 K.
   c) Sidelobe-free spatial response function (equivalent to 100% beam efficiency), resulting from innovative deconvolution in ground processing.
4) The instrument is reconfigurable on-orbit.
   a) Channel frequencies and integration times can be changed by command.
      a) This enables hyperspectral sounding and increased vertical resolution in the boundary layer.
5) The GeoSTAR instrument concept has been matured during many years of development effort, and technology risks have been retired.
   a) The system is at TRL 6, verified by JPL technology assessment board.
   b) A GEO MW mission is therefore of low risk.

6) A wide trade space makes several implementation options possible.

    a) A "small" version with a 1000-km FOV is steerable for target tracking and is suitable for hosting on a communications satellite.

    b) A larger version has a 5000-km FOV.

    c) An even larger "legacy" version implements AMSU and ATMS channels.

REFERENCES

[1] H. E. Montgomery and L. W. Uccellini, *VAS Demonstration: (VISSR Atmospheric Sounder) Description* (No. NASA-RP-1151), 1985.

[2] R. Anthes and B. Moore, Eds. *Earth Science and Applications From Space—National Imperatives for the Next Decade and Beyond*. Washington, DC, USA: National Academies, 2007.

[3] B. Lambrigtsen, T. Gaier, P. Kangaslahti, B. Lim, A. Tanner, and C. Ruf, "Enabling the NASA decadal-survey 'PATH' mission," in *Proc. IEEE Int. Geosci. Remote Sens. Symp.*, 2016, pp. 3949–3951.

[4] S. Q. Kidder *et al.*, "Satellite analysis of tropical cyclones using the advanced microwave sounding unit (AMSU)," *Bull. Amer. Meteorol. Soc.*, vol. 81, no. 6, pp. 1241–1260, 2000.

[5] T. Zhu, D. L. Zhang, and F. Weng, "Impact of the advanced microwave sounding unit measurements on hurricane prediction," *Monthly Weather Rev.*, vol. 130, no. 10, pp. 2416–2432, 2002.

[6] A. Tanner *et al.*, "Initial results of the geostationary synthetic thinned array radiometer (GeoSTAR) demonstrator instrument," *IEEE Trans. Geosci. Remote Sens.*, vol. 45, no. 7, pp. 1947–1957, Jul. 2007.

[7] A. Tanner *et al.*, "Field tests of the GeoSTAR demonstrator instrument," in *Proc. IEEE Int. Geosci. Remote Sens. Symp .*, 2007, pp. 2427–2430.

[8] A. Tanner, T. Gaier, W. Imbriale, P. Kangaslahti, B. Lambrigtsen, and B. Lim, "A dual-gain design for the geostationary synthetic thinned array radiometer," *IEEE Geosci. Remote Sens. Lett.*, vol. 11, no. 8, Aug. 2014, pp. 1340–1344.

[9] M. Minamide and F. Zhang "An adaptive background error inflation method for assimilating all-sky radiances," *Quart. J. Roy. Meteorol. Soc.*, 2019; vol. 145, pp. 805–823, doi: 10.1002/qj.3466.

[10] D. S. Nolan, R. Atlas, K. T. Bhatia, and L. R. Bucci, "Development and validation of a hurricane nature run using the joint OSSE nature run and the WRF model," *J. Adv. Model. Earth Syst.*, vol. 5, no. 2, pp. 382–405, 2013.

[11] S. Tanelli *et al.*, "Integrated instrument simulator suites for earth science," in *Proc. SPIE 8529, Remote Sens. Model. Atmos., Oceans, Interact. IV*, Nov.–Aug. 2012, p. 85290D.

[12] M. I. Mishchenko, *Scattering, Absorption, and Emission of Light by Small Particles*, Cambridge, U.K.: Cambridge Univ. Press, 2002.

[13] B. T. Draine and P. J. Flatau,. 1994, "Discrete dipole approximation for scattering calculations," *J. Opt. Soc. Amer. A*, vol. 11, pp. 1491–1499.

[14] A. Battaglia, and S. Tanelli, "DOMUS: DOppler multiple-scattering simulator," *IEEE Trans. Geosci. Remote Sens.*, vol. 49, no. 1, pp. 442–450, Jan. 2011.

[15] Q. Liu, F. Weng, and S. English, "An improved fast microwave water emissivity model," *IEEE Trans. Geosci. Remote Sens.*, vol. 49, pp. 1238–1250, 2011.

[16] C. W. O'Dell, A. K. Heidinger, T. Greenwald, P. Bauer, and R. Bennartz, "The successive-order-of-interaction radiative transfer model, Part II: Model performance and applications," *J. Appl. Meteor. Climatol.*, vol. 45, pp. 1403–1413, 2006. doi: 10.1175/JAM2409.1.

[17] I. Yanovsky, B. Lambrigtsen, A. Tanner, and L. Vese, "Efficient deconvolution and super-resolution methods in microwave imagery," *IEEE J. Sel. Topics Appl. Earth Observ. Remote Sens.*, vol. 8, no. 9, pp. 4273–4283, May 2015, doi: 10.1109/JSTARS.2015.2424451.

[18] N. Smith and C. D. Barnet, "Uncertainty characterization and propagation in the community long-term infrared microwave combined atmospheric product system (CLIMCAPS)," *Remote Sens.*, vol. 11, no. 10, p. 1227, 2019.

[19] B. Lambrigtsen, H. Van Dang, F. J. Turk, S. M. Hristova-Veleva, H. Su, and Y. Wen, "All-weather tropospheric 3-D wind from microwave sounders," *IEEE J. Sel. Topics Appl. Earth Observ. Remote Sens.*, vol. 11, no. 6, pp. 1949–1956, Jun. 2018.

[20] C. S. Velden and D. Herndon, "A consensus approach for estimating tropical cyclone intensity from meteorological satellites: SATCON," *Weather Forecasting*, vol. 35, no. 4, pp. 1645–1662, 2020.

[21] D. Posselt, B. Lambrigtsen, M. Minamide, M. Schreier, J. Roman, and L. Wu, "Assessing the forecast impact of a geostationary microwave sounder using regional and global OSSEs," in press, *Monthly Weather Rev.*, 2021.

Bjorn Lambrigtsen received the B.S. degree in physics from the Norwegian Institute of Technology, Trondheim, Norway in 1967 and pursued graduate work in physics with the University of Southern California, Los Angeles, CA, USA, in 1969–1979.

Since 1982, he has been with the Jet Propulsion Laboratory, Pasadena, CA, USA, where he is currently a Principal Scientist and leads the Atmospheric Physics and Weather Group. He specializes in atmospheric remote sensing and related research, with a focus on infrared and microwave sounding, and is the Microwave Instrument Scientist for the Atmospheric Infrared Sounder satellite project. He is the GeoSTAR Principal Investigator and leads a number of other research efforts. He has participated in a number of hurricane field campaigns. His research interests include tropical cyclones.

Pekka Kangaslahti (Member, IEEE) received the M.Sc. and Ph.D. degrees from Aalto University (formerly the Helsinki University of Technology), Espoo, Finland, in 1992 and 1999, respectively.

He is currently a Group Supervisor and a Principal Engineer with the Microwave Systems Technology Group, Jet Propulsion Laboratory, California Institute of Technology, Pasadena, CA, USA. His research interests include development of millimeter-wave and submillimeter-wave monolithic microwave integrated circuits, modules, receivers, and receiver arrays.

Oliver Montes received the B.S. and M.S. degrees in electrical engineering from University of California, Los Angeles, CA, USA, in 2007 and 2010, respectively.

He is currently the RF Lead for the Microwave Electrojet Magnetogram instrument of the Electrojet Zeeman Imaging Explorer Mission. He has been involved with several spaceborne and airborne radiometer instruments, including the NASA Juno Microwave Radiometer instrument, the Advanced Microwave Radiometers on Jason-3 and Sentinel-6, and the U.S. Air Force Compact Ocean Wind Vector Radiometer instrument that is being deployed on the International Space Station. He was the Electronics Lead for the Mars2020 Rover SHERLOC instrument and Electrical Systems Engineer for the NASA Multi-Angle Imager for Aerosols instrument. His research interests include microwave radiometer implementation and the design of MMIC amplifiers and other microwave components.

Noppasin Niamsuwan received the Ph.D. degree in electrical engineering from the Ohio State University, Columbus, OH, USA, in 2009.

He is a Signal Analysis Engineer and a Science Application Specialist with experience in software development in various roles on both commercial and scientific products. He was a System Architect and a Task Manager for NASA Earth Observing Systems Simulator Suite (NEOS3), leading the team of application developers and modeling experts to build an extensible instrument simulator suite that helps design a new instrument and its observation strategy. He is currently a Radar System Engineer supporting NISAR (NASA-ISRO Synthetic Aperture Radar) mission, leading the analysis of L-band radar instrument for system integration and testing. His research interests include microwave remote sensing of the Earth's surface and atmosphere, electromagnetic wave theories and applications, and simulation of microwave remote sensing system.

Derek J. Posselt received the B.S. and M.S. degrees in atmospheric science from the University of Wisconsin, Madison, WI, USA in 1997 and 2001, respectively, and the Ph.D. degree in atmospheric science from Colorado State University, Fort Collins, CO, USA, in 2006.

He was a Professor with the University of Michigan, Ann Arbor, MI, USA from 2007 to 2016. Since 2016, he has been a Scientist with the Atmospheric Physics and Weather Group, NASA Jet Propulsion Laboratory, Pasadena, CA, USA. He was the Cyclone Global Navigation Satellite System (CYGNSS) Deputy Principal Investigator from 2012 to 2016, and is the Co-Lead of the Modeling and Data Assimilation working group for the Atmosphere Observing System (AOS) mission. He has served as a science team member for the CYGNSS, CloudSat, and Precipitation Measurement Mission (PMM) missions. His research interests include observation and modeling of cloud and precipitation processes, satellite remote sensing and data assimilation, and observing system simulation experiments.

Jacola Roman received the Ph.D. degree in atmospheric and oceanic sciences from the University of Wisconsin Madison, WI, USA, in 2016.

She was an Assistant Teaching Professor with the Dutton E-Education Institute and the Department of Meteorology and Atmospheric Science, Pennsylvania State University, where she developed a Weather and Climate Analytics graduate program. Since 2019, she has been with the Physics and Weather Group, Jet Propulsion Laboratory, Pasadena, CA, USA. She has been involved in assessing and validating remotely sensed NASA products for AIRS and SIPS. Her research interest includes retrieval validation, weather and climate analytics, and trend detection.

Mathias Schreier received the M.S. degree in meteorology from the University of Munich, Munich, Germany, and the Ph.D. degree in atmospheric physics from the University of Bremen, Bremen, Germany, in 2008.

He was a Postdoctoral Fellow and Assistant Researcher with the University of California, Los Angeles, CA, USA, from 2009 to 2013 within the JIFRESSE program (Joint Institute for Regional Earth System Science & Engineering). Since 2013, he has been a Research Scientist with the Jet Propulsion Laboratory, Pasadena, CA, USA. He is currently working on retrieval approaches for microwave instruments and Co-Lead for the development of JPSS and SNPP sounder products. His research interests include infrared and microwave sounding from airborne instruments and from space, combined with synergistic uses of these sounder products in connection with cloud and atmospheric products from other instruments.

Alan Tanner received the Ph.D. degree from the University of Massachusetts, Amherst, MA, USA, in 1989.

His graduate school and professional work have focused on the design and applications of microwave and millimeter-wave radiometers and radars for remote sensing of the Earth. Since 1989, he has been with Jet Propulsion Laboratory, Pasadena, CA, USA. He has been the lead Engineer for the Geostationary Synthetic Thinned Array Radiometer (GeoSTAR) prototypes, the Ultra-Stable Radiometer testbed (which formed the basis of the Aquarius and Juno radiometer designs), the Advanced Water Vapor Radiometers (AWVR) for the Cassini Gravitational Wave Experiment, the Airborne Cloud Radar (a 94-GHz scatterometer which preceded the CloudSat mission), and the Airborne Rain Mapping Radar (for Tropical Rainfall Measurement Mission). He developed the Electronically Scanned Thinned Array Radiometer (ESTAR) for soil moisture measurements, and the Stepped Frequency Microwave Radiometer (SFMR) for hurricane wind-speed detection from NOAA reconnaissance aircraft.
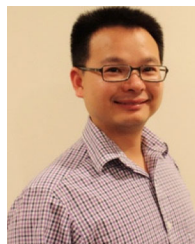
Longtao Wu received the B.S. and M.S. degrees in atmospheric science from Peking University, Beijing, China, in 2001 and 2004, respectively, and the Ph.D. degree from the Department of Atmospheric and Oceanic Sciences, University of Wisconsin-Madison, Madison, WI, USA, in 2010.

From 2010 to 2011, he was a Postdoctoral Scholar with the Jet Propulsion Laboratory, Pasadena, CA, USA, where he is currently a Data Scientist. He was an Assistant Researcher with the University of California, Los Angeles from 2012 to 2014. His research interests include numerical simulation of the weather and climate systems, observing system simulation experiments, tropical cyclone, and machine learning.

Igor Yanovsky received the B.S. and M.A. degrees in 2002, and the Ph.D. degree in 2008 from the University of California, Los Angeles, CA, USA, all in applied mathematics.

He has been with NASA Jet Propulsion Laboratory, California Institute of Technology, Pasadena, CA, USA, since 2008, where he is currently a Data Scientist. He was with the Joint Institute for Regional Earth System Science and Engineering at the University of California, Los Angeles, CA, USA, from 2011 to 2021. Since 2021, he is an Associate Project Scientist at the Department of Mathematics at the University of California, Los Angeles, CA, USA. His research interests include formulation and development of computational algorithms for solving inverse problems in data science, remote sensing, and image processing.